PAPER

A zeolitic imidazolate framework (ZIF-67) and graphitic carbon nitride (g-C$_3$N$_4$) composite based efficient electrocatalyst for overall water-splitting reaction†

Sadia Khan, [a] Tayyaba Noor, *[a] Naseem Iqbal, [b] Erum Pervaiz [a] and Lubna Yaqoob[b]

Designing of non-noble, cost-effective, sustainable catalysts for water splitting is essential for hydrogen production. In this research work, ZIF-67, g-C$_3$N$_4$, and their composite (1, 3, 5, 6, 8 wt% g-C$_3$N$_4$@ZIF-67) are synthesized, and various techniques, XRD, FTIR, SEM, EDX and BET are used to examine their morphological properties for electrochemical water-splitting. The linkage of ZIF-67 with g-C$_3$N$_4$ synergistically improves the electrochemical kinetics. An appropriate integration of g-C$_3$N$_4$ in ZIF-67 MOF improves the charge transfer between the electrode and electrolyte and makes it a suitable option for electrochemical applications. In alkaline media, the composite of ZIF-67 MOF with g-C$_3$N$_4$ over a Ni-foam exhibits a superior catalyst activity for water splitting application. Significantly, the 3 wt% g-C$_3$N$_4$@ZIF67 composite material reveals remarkable results with low overpotential values of -176 mV@10 mA cm^{-2}, 152 mV@10 mA cm^{-2} for HER and OER. The catalyst remained stable for 24 h without distortion. The 3 wt% composite also shows a commendable performance for overall water-splitting with a voltage yield of 1.34 v@10 mA cm^{-2}. The low contact angle (54.4°) proves the electrocatalyst's hydrophilic nature. The results of electrochemical water splitting illustrated that 3 wt% g-C$_3$N$_4$@ZIF-67 is an electrically conductive, stable, and hydrophilic-nature catalyst and is suggested to be a promising candidate for electrochemical water-splitting application.

1. Introduction

Energy is essential for any developed society to grow their economy and industry. Currently, energy is produced by fossil fuels, which generates environmental hazards, and besides this, the dwindling reserves of fossil fuels cannot meet modern society's demands.[1–5] Therefore, researchers intend to produce energy from renewable natural resources. Green hydrogen is an environmentally friendly and sustainable energy source compared to fossil fuels. Among all the natural resources (air, water, solar, geothermal), hydrogen energy produced by water electrolyzing has been declared a future power fuel due to its sustainability, high energy density, and green characteristics.[6–8] Hydrogen produced by water-splitting is used as a fuel in a hydrogen fuel cell to generate electricity through an electrochemical reaction and can be used to power various applications, such as vehicles, buildings, and electronic devices.[9–11]

The water-splitting process comprises two half-cell reactions; oxygen evolution reaction (OER) which occurs at the anodic side and hydrogen evolution reaction (HER), which occurs at the cathode side of the cell.[12–15] In the process, OER is more complex as compared to HER. The four-electron anodic process OER comprises the formation of O–O bond and dissociation of the O–H bond at a specific current density, which is thermodynamically slow and affects the overall rate of the water-splitting reaction. So catalyst is required to enhance the kinetics.[16] Previously, noble metals (Pt, Pd, and Rd) are used as a catalyst for the HER and OER processes to conquer the complex bonding of the molecules and enhance the kinetics. But their poor stability and the high cost are hurdles to commercialization. Commercially available Pt/C catalysts suffer erosion resistance that may cause the distortion of Pt and carbon particles to produce the aggregate. Therefore catalysts cannot retain stability for a long time, which is another drawback of expensive materials. Thus, scientists are trying to dig out the abundantly available non-precious, efficient, durable metal catalyst for water-splitting activity.[17–20] Moreover, there are three main challenges for the researchers to design an efficient electrocatalyst (1) improvements required in interfacial characteristics, (2) a high surface-to-volume ratio required, (3) a high density of active sites required to improve mass and charge transfer. In recent years, there has been

School of Chemical and Materials Engineering (SCME), National University of Sciences and Technology (NUST), Islamabad 44000, Pakistan. E-mail: tayyaba.noor@scme.nust.edu.pk; Tel: +92 51 90855121

U.S.-Pakistan Center for Advanced Studies in Energy (USPCAS-E), National University of Sciences and Technology (NUST), Islamabad 44000, Pakistan

a growing interest in transition metal catalysts, particularly those belonging to the Fe, Co, and Ni series. These transition metal catalysts hold great promise as they are expected to exhibit comparable activity to noble metal catalysts. Transition metal-based chalcogenides, nitride, and carbide materials also proved an efficient catalyst for electrochemical applications.[21] Furthermore, 3-D Transition metals (Zn, Co, Fe, Ni) based metal–organic frameworks (MOF) materials are considered promising catalysts due to their significant activity in water electrolysis over the last two decades.[22,23] MOFs are fabricated by the incorporation of metal ions along with organic ligands. Metal–organic framework (MOF) based catalysts are in crystalline form, have a dynamic structure, acquire a large surface area (6000 m^2 g^{-1}), have more flexibility, and have high porosity (90 percent free volume). Owing to all these properties, MOFs are used as a catalyst in energy storage devices, Li-ion batteries, fuel cells, and water-splitting applications.[24–26] MOF-based catalysts can be synthesized *via* simple interlocking inorganic metals with organic material, which have high porosity and are inherently flexible. In this essence, Maryam *et al.* (2021) designed a UiO/MoC$_2$ MOF for a water-splitting application. They reported an overpotential 310 mV@20 mA cm^{-2} for OER and 37 0 mV@10 mA cm^{-2}. They described that MOFs possess a high crystallinity, huge surface area, and void porosity (90%), which support and sustain the electrochemical water-splitting reaction.[27] Yaqoob *et al.* designed FeNi/CNT MOF *via* a solvothermal process for OER activity and attained superior results with a low overpotential of 0.22 V to achieve a current density of 10 mA cm^{-2}. The kinetics of the MOF increased due to the presence of nickel oxides (hydroxide) interconnection with iron. The lattice structure was more conductive due to high stain and less resistance.[28] Noor *et al.* reported that low-cost cobalt metal present in different oxidation states (Co^{2+}, Co^{3+}), is beneficial for hydrogen production especially giving robust result for OER activity with low overpotential 0.29 V to attain the current density 10 mA cm^{-2}.[29] Cobalt has high hydrogen binding energy "ΔE_H*" for HER, similar to Pt, and can produce oxy/hydroxide during the OER process. Its linkage with organic ligands behaves like an N-doping which can promote the conductivity into carbonaceous-matrix.[30–32] ZIF-67 MOF, constructed by cobalt ion metal and 2-methylimidazole ligand, gained much attention for electrochemical water-splitting applications due to its intrinsic properties. ZIF67 MOF contains a high surface area and flexible porous structure and is an efficient catalyst for electrochemical applications. Additionally, ZIFs (Zeolitic Imidazolate Frameworks) possess a high carbon, nitrogen, and active center metals content, contributing to their remarkable catalytic activity.[33–35] In this regard, in 2018, Wang *et al.* synthesized ZIF-67 *via* a simple stirring method. The designed MOF is active for the OER; it required a 540 mV "overpotential" to achieve the "current density" of 10 mA cm^{-2}, while the Tafel slope value is 125.5 mV dec^{-1} by using the glassy carbon working electrode.[36] In 2019, Guo *et al.* synthesized ZIF-67 by the simple stirring method at room temperature; the designed MOF is active for the OER in the presence of alkaline media (3MKCl) with 408 mV "overpotential," and the Tafel slope value is 128.2 mV dec^{-1} to attain current density 10 mA cm^{-2}.[37]

In addition, the collaboration of MOF with carbonaceous material (g-C$_3$N$_4$, rGO, CNT) increases the material's mechanical strength. Therefore, to enhance the strength and conductivity of the ZIF, many researchers declared that non-precious carbonaceous materials such as carbide, nitride, phosphide, and sulfide, based compounds might improve the morphology, structural composition, electrical conductivity, and stability of the MOF.[38–40] Furthermore, the literature shows that g-C$_3$N$_4$ (graphitic carbon nitride) is the best choice for improving the catalyst's electronic configuration and stability of the MOF.[41] Graphitic carbon nitride is the most stable carbon–nitrogen-based allotrope in water-based solvents. Moreover, the polymeric nature of g-C$_3$N$_4$ contains a flexible structure and can host any inorganic-based compound.[42,43] In this regard, in 2019, Wang *et al.* designed a coral-like structure nanomaterial of NiSe$_2$ on the support of graphitic-carbon nitride (g-C$_3$N$_4$). The nanocomposite showed superb performance for the OER with a low "overpotential" of 290 mV to attain a "current density" (*j*) of 40 mA cm^{-2}, and the catalyst remained durable for approximately 40 h.[44] It is noticed that N-doped carbon provides the best electron transportation facility.[45] Hence, the graphitic-carbon nitride (g-C$_3$N$_4$) is a reliable source of N-riched carbon, and a non-precious, metal-free, highly stable catalyst that can be prepared by a simple method.[46] Thus, modified mesoporous g-C$_3$N$_4$ significantly improves the kinetics of the process by rapid charge transfer and is suitable as a co-catalyst for water-splitting activity.[47,48] In 2021, Li *et al.* designed an electrocatalyst nanosheet FeS$_2$/MoS$_2$ to support graphitic-carbon nitride (g-C$_3$N$_4$) by the hydrothermal method. The bridging composite has a large surface active area for the charge transferring and showed a remarkable catalytic efficiency with a low "overpotential" of 190 mV at 10 mA cm^{-2} for the HER and remained stable for 10 h.[49]

Deposing a catalyst on a 3D electrode like Ni foam is also an effective strategy to promote the kinetics of the reactions. For illustration, in 2022, Zahra *et al.* designed a flower-like CoNi$_2$S$_4$/g-C$_3$N$_4$ MOF using the hydrothermal method at the Ni foam. The designed MOF is used as an excellent bifunctional catalyst. The results of HER and OER showed very low "overpotential"; for OER (310 mV) and HER (160 mV) are required in the alkaline media, which proved that the kinetic of the catalyst improved on the backbone of Ni-foam.[50]

Meng *et al.* designed a composite of g-C$_3$N$_4$/ZIF-67 by encapsulating ZIF-67 with g-C$_3$N$_4$. They stated that g-C$_3$N$_4$ in the composite material plays a dual role, used as an electron acceptor to promote the charge transfer and as an effective co-catalyst to accelerate the reaction. So the combination of ZIF-67 with graphitic carbon nitride not only enhances the specific surface area but also improves the catalyst activity.[51]

Based on the constructive ideas outlined above, we synthesize composites of 1, 3, 5, 6, and 8 wt% g-C$_3$N$_4$@ZIF-67 for water-splitting applications in this research work. According to our knowledge, prior publications have yet not report the specific combination and optimized amount of g-C$_3$N$_4$ with ZIF-67 for overall water-splitting. For this purpose, by varying the proportion of g-C$_3$N$_4$ within the composite, we aim to identify the optimal ratio that maximizes the catalytic activity. In light of

the literature review, designed composites will provide high catalytic activity and stability for water-splitting applications.

2. Experimental section

2.1. Materials

For the synthesis of ZIF-67, reagents are cobalt-nitrate hexahydrate (99.99% pure), 2-methylimidazole (99% pure), and deionized water (18 MΩ cm) purchased from Sigma-Aldrich. In addition, melamine (99% pure) is required to synthesize graphitic-carbon nitride (g-C$_3$N$_4$) purchased from Sigma-Aldrich. Nafion 117 solution (5% in a mixture of lower aliphatic alcohols and water), propanol (99.8% pure) and ethanol (99.8% pure) for catalyst ink preparation reagents are purchased from Merck. All the chemicals are purified; no further processing is required.

2.2. Synthesis of ZIF-67

ZIF-67 is synthesized as the previously reported method by Qian et al.[52] As shown in Fig. 1, for the fabrication of ZIF-67, the simple stirring method is adopted; for this, two solutions are prepared, followed by magnetic stirring. The first metal solution is organized by mixing Co(NO$_3$)$_2$·6H$_2$O (0.45 g) into DI water (3 ml). The second

linker solution is prepared by blending 2-methyl imidazole (CH$_3$-C$_3$H$_2$N$_2$H) (5.5 g) into DI water (20 ml). After continuous (20 min) stirring, the linker solution is gradually added to the metal solution. The two homogeneous solutions are stirred through a magnetic stirrer for 6 h at ambient temperature. After centrifuging, the purple precipitates are collected and washed with methanol and DI water. The final product is dried overnight in a vacuum oven at 80 °C.[52]

2.3. Synthesis of g-C$_3$N$_4$

The graphitic-carbon nitride is synthesized by pyrolysis of melamine under the argon atmosphere. Take 1 g of melamine filled into the combustible porcelain boat and put it into the tube furnace at 600 °C by increasing the rate to 5 °C min^{-1} for 6 h. After the completion of the process, a pale yellow color product is obtained, as shown in Fig. 2.[53]

2.4. Synthesis of 1, 3, 5, 6, 8 wt% composite of ZIF-67/g-C$_3$N$_4$

The hydrothermal method is adopted for synthesizing composite materials 1, 3, 5, 6, 8 wt% g-C$_3$N$_4$@ZIF-67, as shown in Fig. 3.[54] First, solution 1 is prepared by adding Cobalt-nitrate hexahydrate (0.45 g) into the 3 ml DI water, stirring it for
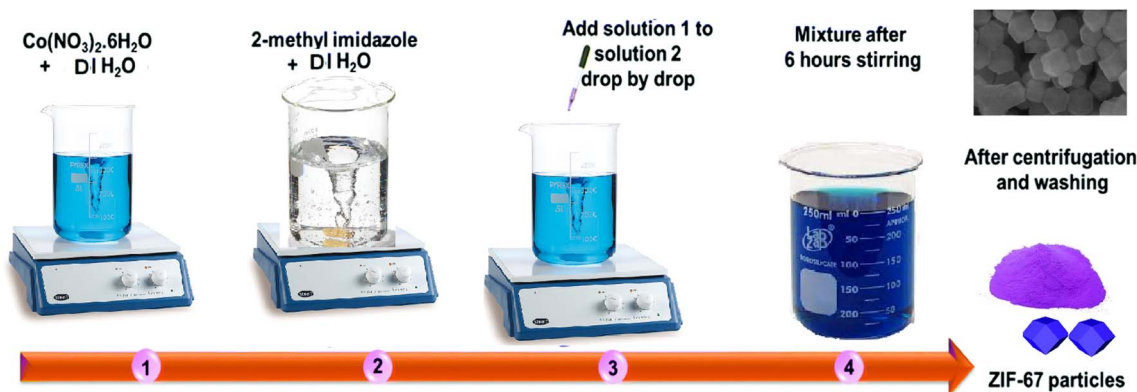

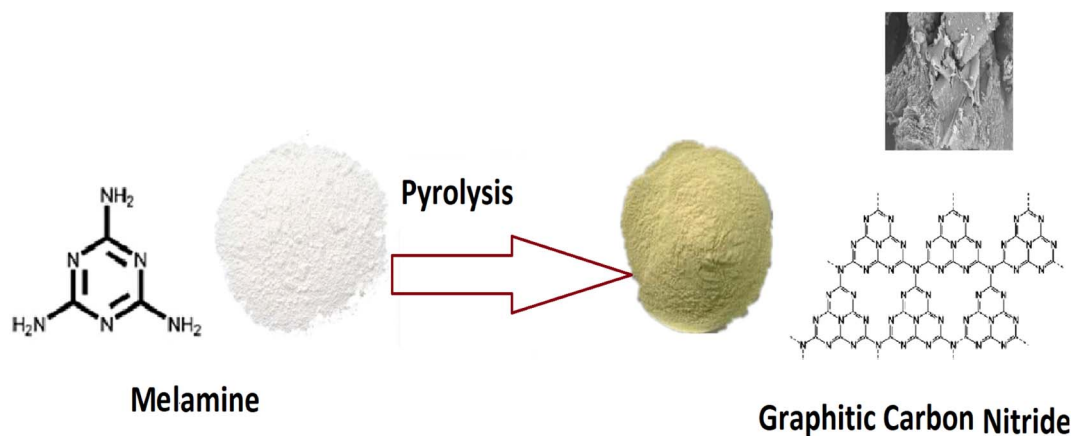Fig. 1   Schematic illustration of the fabrication of ZIF-67 MOF.

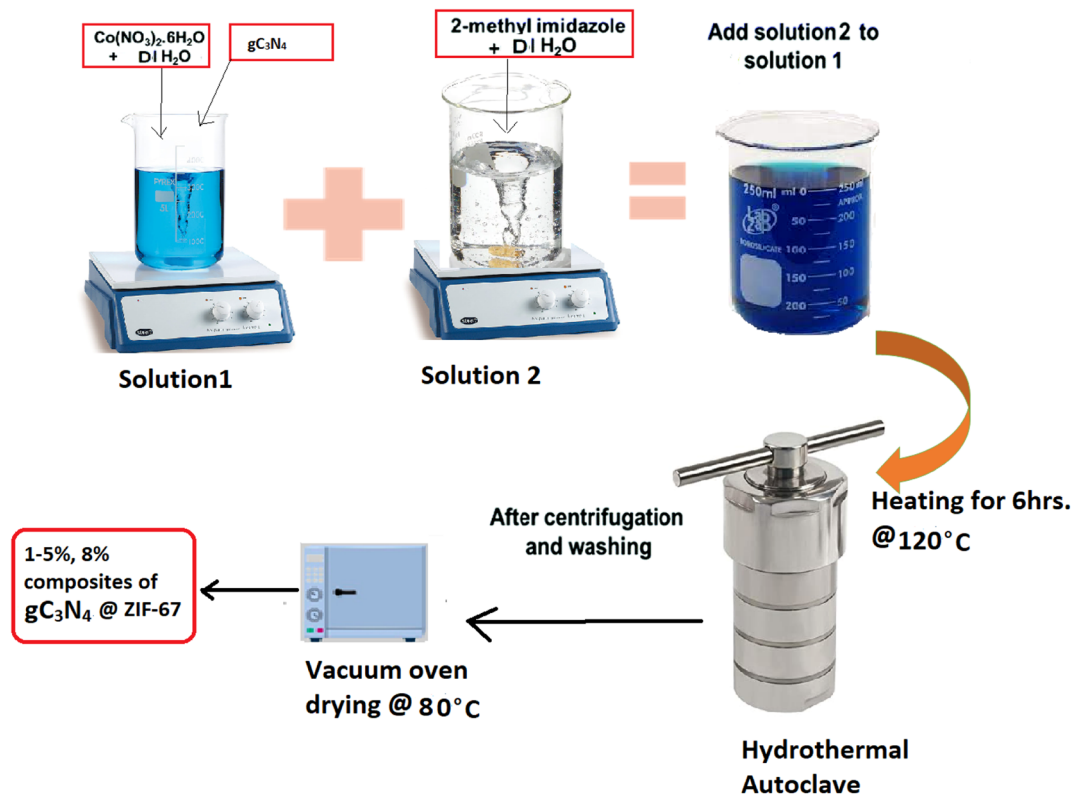Fig. 2   Synthesis of g-C$_3$N$_4$ from melamine by pyrolysis.

Fig. 3 Schematic showing the synthesis procedure of 1, 3, 5, 6, 8 wt% g-C_3N_4@ZIF-67 composite.

10 min, then introducing g-C_3N_4 in different mass ratios (1 wt%, 3 wt%, 5 wt%, 6 wt% and 8 wt%) into the solution 1, followed by continuous stirring. After 20 min of stirring, solution 2 (5.5 g of 2-methylimidazole into 20 ml DI) is added into solution 1 and stirred for 1 h continuously. Then the homogeneous solution is transferred into the Teflon autoclave at 120 °C for 6 h. After the accomplishment of the reaction product is repeatedly washed with methanol and DI water through centrifugation and dried in the vacuum oven at 80 °C overnight.[54–56]

2.5. Physical characterization

The crystalline structure was examined by X-ray powder diffraction (XRD) of the composite. XRD STOE German machine linked with computer and provided CuKα radiation @ λ = 0.154 nm, diffraction angle 0°–70° and step size 4° s^{-1}. Scanning electron microscopy (SEM) VEGA3 TASCON, armed with elemental dispersive spectroscopy (EDS), was used to examine the morphology of the catalyst surface at various resolutions and determine the material's composition. In addition, Fourier Transform infrared spectroscopy (FTIR – Perkin Spectrum) was used to investigate the metal–ligand coordination within the wave number of 500–4000 cm^{-1}.

2.6. Electrochemical analysis

The electrocatalyst performance is measured in the presence of 1.0 M KOH electrolyte solution using the three electrodes (counter, reference, and working) assembled in the cell. The reference electrode is an Ag/AgCl electrode, the Graphite

electrode is counter, and Ni-foam coated with catalyst ink is the working electrode. A Gamry potentiostat workstation is used to examine the electrocatalyst activities. Different techniques, such as cyclic voltammetry, linear sweep voltammetry, chronopotentiometry, and electrochemical impedance spectroscopy, are used for electrochemical testing. Cyclic voltammetry measurements are reported at 10 mV s^{-1} in the specific potential range of 0.9–1.7 V *vs.* RHE for redox reaction. The linear sweep voltammetry is accomplished for OER and HER over a potential range of 0 to −0.6 (V *vs.* RHE) for HER and 1.1 to 1.6 (V *vs.* RHE) for OER at a scan rate of 10 mV s^{-1} to measure the overpotential.

The potential is converted to a reversible hydrogen electrode (RHE) for standardization by eqn (1)

$$E_{RHE} = E_{Ag/AgCl} + 0.059_{pH} + E^0_{Ag/AgCl} \qquad (1)$$

where $E^0_{Ag/AgCl} = 0.1976$ and pH = 14.

For Tafel plots, "overpotential" is plotted on the *y*-axis, and the logarithm of current density is on the *x*-axis. By eqn (2), the slope is calculated.

$$\eta = b \log I + a \qquad (2)$$

where "η" represent the "overpotential," "I" is "current density," while "b and a" are the Tafel constants.

Electrical impedance spectroscopy (EIS) is another fundamental technique that reveals charge transfer resistance (R_{ct}), solution resistance at the interface of electrode and electrolyte

(Ru) electrical conductance in Farad employing a Nyquist plot; the system analysis response contains information about structures and reactions occurring at the interface.

2.7. Working electrode preparation

The preparation of the working electrode involved several steps. Initially, a nickel foam measuring 1×1 cm^2 was thoroughly washed using a sequence of 2 M HCl, ethanol, and DI water. The cleaned nickel foam was then dried at 60 °C. For the catalyst ink, a mixture was created by combining 10 mg of the active catalyst with a solution consisting of 24 μl Nafion and a 1 : 1 ratio of propanol and water (1024 μl), using ultrasonication to ensure homogeneity. Subsequently, 90 μl of the catalyst ink was gently drop-cast onto the nickel foam, ensuring an even distribution. Lastly, the working electrode was dried in a vacuum oven at 70 °C to eliminate residual solvent and facilitate catalyst bonding. Following these steps, a well-prepared working electrode with the catalyst immobilized on the nickel foam surface was obtained.[57]

3. Result and discussion

The structure of synthesized ZIF-67, g-C$_3$N$_4$, and the composite of 1, 3, 5, 6, 8 wt% g-C$_3$N$_4$@ZIF-67/were analyzed by XRD. In Fig. 4, the most prominent diffraction peaks at 7.2°(011), 10.4°(002), 12.7°(112), 14.7°(022), 16.4°(013), 18°(222), 22.1°(114) indicated that crystalline structure ZIF-67 MOF is successfully fabricated.[52,58,59] The formation of the crystalline structure of graphitic carbon nitride is confirmed by the two diffraction peaks at 27.4°(002) and 13.4°(100), as shown in Fig. S1 (ESI†). These two peaks indicate the presence of tri-s-triazine (C$_6$N$_7$), which has high interplanar space and is associated with an aromatic system and confirm the presence of graphitic-carbon nitride (g-C$_3$N$_4$).[60,61] XRD results reveal that ZIF-67 and g-C$_3$N$_4$ have their prominent characteristic peaks, which shows that both the samples are successfully synthesized.[58,60–62] The diffraction peaks of composite materials (g-C$_3$N$_4$@ZIF-67) illustrated that the structure of ZIF-67 would not destroy with the addition of g-C$_3$N$_4$. However, it is noticed that as the amount of graphitic-carbon nitride (g-C$_3$N$_4$) increases, the composite peaks slightly convert into an amorphous phase. It is also observe that during composite formation material became porous and main characteristic peak of g-C$_3$N$_4$ at 27.4°(002) became prominent as the dosage of g-C$_3$N$_4$ increased in the composite but simultaneously, the low angle peak of g-C$_3$N$_4$ at 13.4° disappears during the composite formation (g-C$_3$N$_4$@ZIF-67), which is attributed to the strong interaction of graphite carbon nitride with ZIF-67 MOF, which deformed the nitride pore structure and changed the hole-to-hole distance.[48,63,64] Meanwhile, it is also observed in the 5, 6, 8% g-C$_3$N$_4$@ZIF-6 that as the quantity of graphitic carbon nitride increases, stress within the zeolite cage structure also increases. This stress may cause a change in atomic arrangements between g-C$_3$N$_4$ and ZIF-67, which produce changes in the lattice constants of the composite material. As a result, the XRD peak corresponding to the (002) plane of g-C$_3$N$_4$ may experience a slight shift, and the intensity of the peaks also decreases. This shift indicates that the zeolite cages in the composite are expanding and undergoing changes in their structure.[51,65]
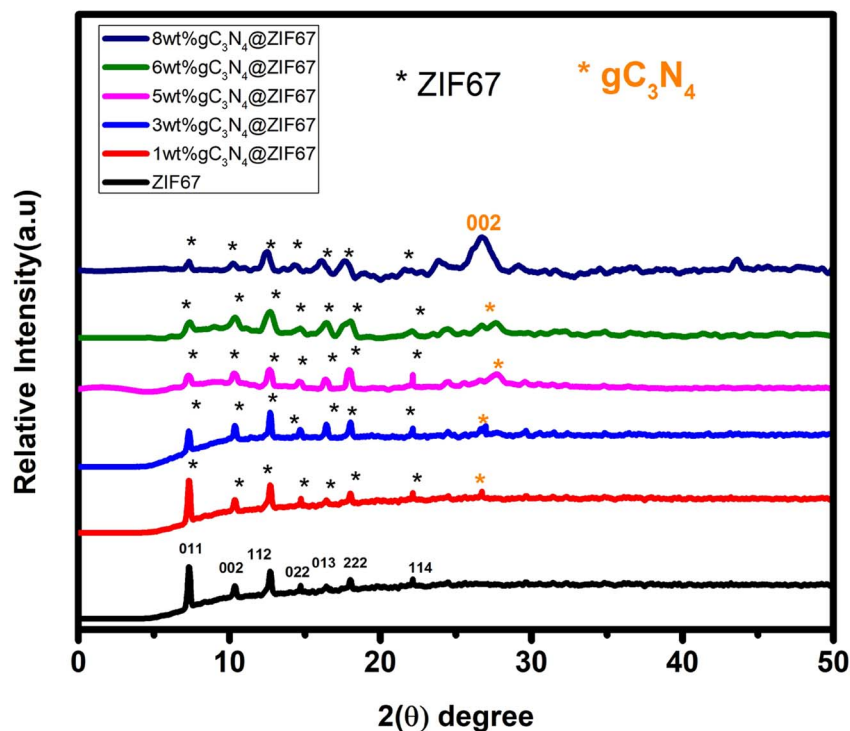

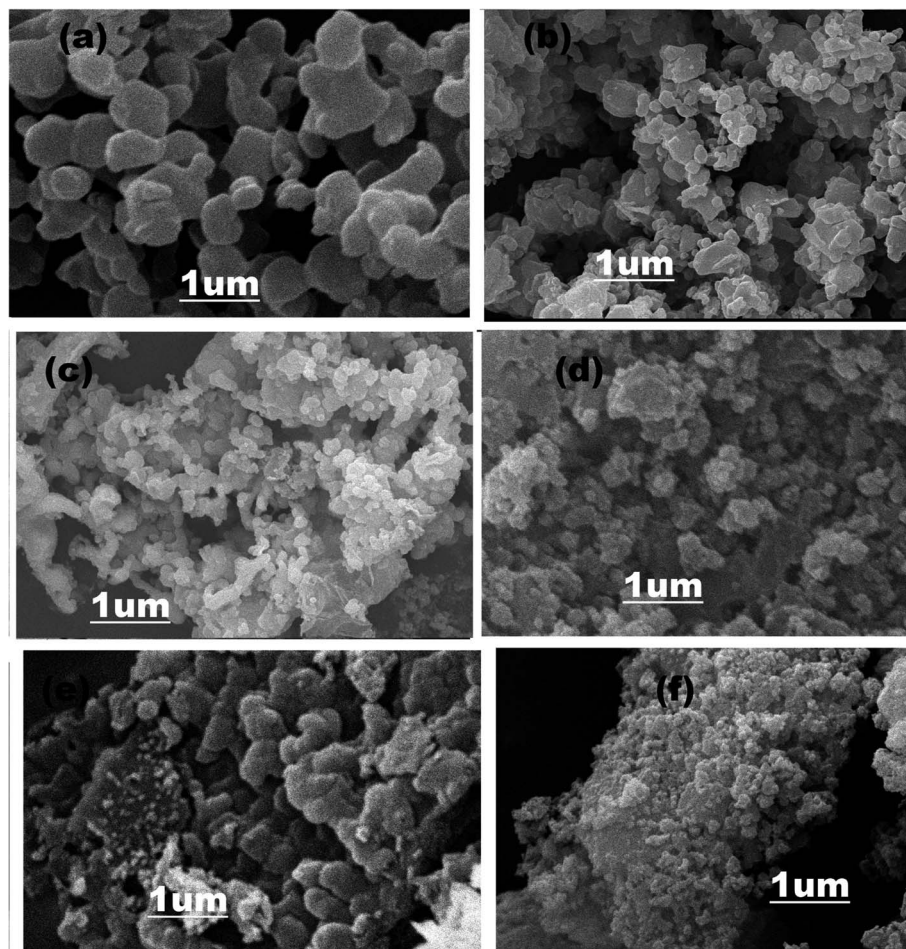Fig. 4 Schematic illustrates the XRD of ZIF-67 MOF, graphitic-carbon nitride (g-C$_3$N$_4$), and composites of 1, 3, 5, 6, 8 wt% g-C$_3$N$_4$ with ZIF-67.

Fig. 5 Schematic illustrates the SEM images of (a) ZIF-67 (b) 1 wt% composite of g-C$_3$N$_4$/ZIF-67 (c) 3 wt% composite of g-C$_3$N$_4$/ZIF-67 (d) 5 wt% composite of g-C$_3$N$_4$/ZIF-67 (e) 6 wt% composite of g-C$_3$N$_4$/ZIF-67 (f) 8 wt% composite of g-C$_3$N$_4$/ZIF-67.

In Fig. 5a, SEM images represent the pure ZIF-67, which acquired a rhombic dodecahedral shape with sharp edges and defined facets.[66,67] The morphology of the g-C$_3$N$_4$ is shown in Fig. S2 (ESI†), representing 2-D sheet-like morphology.[68] SEM images of composite material in Fig. 5b–f illustrated that as different quantities (1, 3, 5, 6, 8 wt%) of g-C$_3$N$_4$ attached with ZIF-67, the morphology of the composite materials converted into the mesoporous structure. By the combination of ZIF-67 with g-C$_3$N$_4$ not only structure of the composite material become porous but also the surface area of the composite material increased that helps to promote the electrochemical water-splitting activity.[51,69,70]

Elemental analysis of the 1, 3, 5, 6, and 8 wt% composite material is examined by elemental diffraction X-ray-

spectroscopy (EDS). The result indicated that composite materials predominantly comprise Co, C, O, and N elements. The elemental mapping is illustrated in Fig. S3 (ESI†), and the composition by wt% of each element is described in Table 1. The result illustrated that composite materials are successfully designed without any impurities.

Nitrogen adsorption–desorption isotherms are employed to determine the synthesized materials' specific surface area and porosity. The BET analysis of 3 wt% g-C$_3$N$_4$@ZIF-67, and ZIF-67 are illustrated in Fig. 6. The IV-type isotherm exhibited a mesoporous structure.[71] It observed that according to the BJH pore size distribution analysis, 3 wt% g-C$_3$N$_4$@ZIF-67 showed a significantly higher BET surface area of 348.2 m^2 g^{-1}, along

Table 1 Elemental analysis of ZIF-67 with 1, 3, 5 wt% g-C$_3$N$_4$ composites

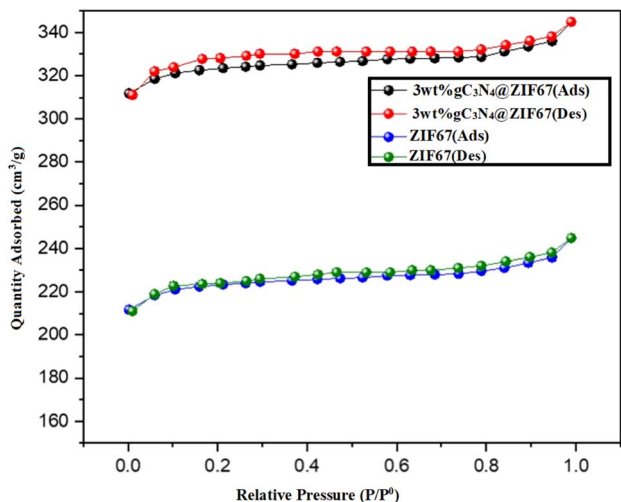| Elements	ZIF-67	1 wt% g-C$_3$N$_4$@ZIF-67	3 wt% g-C$_3$N$_4$@ZIF-67	5 wt% g-C$_3$N$_4$@ZIF-67	6 wt% g-C$_3$N$_4$@ZIF-67	8% g-C$_3$N$_4$@ZIF-67	g-C$_3$N$_4$
C	40.1	41.4	41.6	42.9	43.1	48.9	28.5
N	34.4	39.7	40.2	41.1	41.7	36.6	71.5
O	3.3	3.2	2.1	2.3	2.4	4.3	
Co	22.3	15.7	16.1	13.1	12.8	11	

Fig. 6 BET analysis of ZIF-67 and 3 wt% g-C$_3$N$_4$@ZIF-67.

with a pore diameter of 3.1 nm as compared to ZIF-67, which contained surface area 245.2 m^2 g^{-1} with pore SIZE diameters of 3.3 nm. The high BET surface area of the composite is attributed to graphitic carbon nitride sheets present with ZIF-67 MOF, and thus additional surface area probably lead to enhanced electrocatalytic activity for water-splitting application.[51,69,70]

In addition, Fourier transform infrared spectroscopy is used to investigate the metal–ligand coordination within the wave number of 500–4000 cm^{-1}. FTIR is used to inspect the functional group in the synthesized materials. In Fig. 7, spectra of ZIF-67 represented the vibrational bands in the 600 to 1500 cm^{-1}, ensuring the presence of an imidazole ring representing the stretching and bending characteristics. The band at 1574 cm^{-1} ascribed the presence of C=N with stretching mode in the 2-mim, The vibrational band at 2921 cm^{-1} indicated the
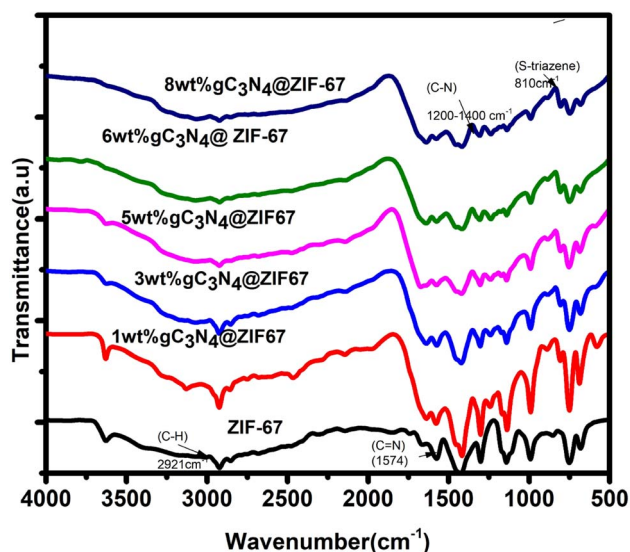

Fig. 7 Schematic illustrates the FTIR spectra of ZIF-67 and composites of 1, 3, 5, 6, 8 wt% g-C$_3$N$_4$@ZIF-67.

C–H stretch aromatic ring of 2-mim and 3130 cm^{-1} attributed the C–H stretching mode of 2 mim in the aliphatic chain[72]. The spectra of g-C$_3$N$_4$ indicated the triazene ring, C–N heterocycle, and an amino group, as shown in Fig. S4.† The peaks at 800 to 889 cm^{-1} exposed that g-C$_3$N$_4$ consists of a triazene ring. At the same time, the region between 1200–1637 cm^{-1} represented the heterocycles C–N (–C)–C stretching, Amino group (N–H) group indicated in the region between 3000–3500 cm^{-1}.[63,73–75] In the spectrum of the composite, significant peaks of ZIF-67 are observed, which showed that the structure of ZIF-67 remained stable. Moreover, it is also observed that as the amount of g-C$_3$N$_4$ increased triazene ring region and C–N heterocycle region become prominent, which shows the presence of g-C$_3$N$_4$ with ZIFMOF without destroying the structure.

3.1. Hydrogen evolution reaction

The HER activity of synthesized electrocatalyst ZIF-67, g-C$_3$N$_4$, and 1, 3, 5, 6 and 8 wt% g-C$_3$N$_4$@ZIF67 are detected by the linear sweep voltammetry (LSV) in the presence of three electrode assembly. For comparison, 5 wt%Pt/c was cast at the Ni-foam with the same procedure. The polarization curves of electrocatalyst ZIF-67, g-C$_3$N$_4$, and 1, 3, 5, 6, and 8 wt% g-C$_3$N$_4$ composites are illustrated in Fig. 8a, which quantify the kinetics. The over-potential of Ni-foam (−0.43 V), ZIF-67 (−0.307 V), g-C$_3$N$_4$ (−0.379 V), 1 wt% g-C$_3$N$_4$ (−0.256 V), 3 wt% g-C$_3$N$_4$ (−0.176 V), 5 wt% g-C$_3$N$_4$ (−0.19 V), 6 wt% g-C$_3$N$_4$(−0.236), 8 wt% g-C$_3$N$_4$ (−0.31) and 5% Pt/c (−0.063 V) are observed to achieve the current density at −10 mA cm^{-2}. Results reveal that 3 wt% composites exhibited the best HER catalyst activity with low overpotential in the alkaline media as compared to designed material, as shown in overpotential bar graph Fig. 8b. 3 wt% composite also performed better for HER as compared to other reported cobalt-based catalysts[76–78] mentioned in Table S1 (ESI†). This is likely due to the 3 wt% composite achieve optimum composition and surface area during synthesizing. However, 5 wt% Pt/c is used as a benchmark for HER, so the 3 wt% g-C$_3$N$_4$@ZIF-67 has a slightly larger value than 5% Pt/c. Similar results achieve to attain the current density of −30 mA cm^{-2}, overpotential of 3 wt% g-C$_3$N$_4$@ZIF-67 is −0.199 V recorded, which is superior to ZIF-67 (−0.335 V), g-C$_3$N$_4$ (−0.415), 1 wt% g-C$_3$N$_4$@ZIF-67 (−0.273 V), 5 wt% g-C$_3$N$_4$@ZIF-67 (−0.214 V), 6 wt% g-C$_3$N$_4$@ZIF-67 (−0.254), 8 wt% g-C$_3$N$_4$@ZIF-67 (−0.38) while for 5% Pt/c overpotential is −0.069 V.

Tafel slope associates with the overpotential reaction rate. A smaller Tafel slope implies quick electron transport. Therefore, a low Tafel slope with a lower "overpotential" is a benchmark for active catalysts. The Tafel slope for HER is shown in Fig. 8c, which represents that ZIF-67 and g-C$_3$N$_4$ attain a Tafel slope of 182 mV dec^{-1} and 254 mV dec^{-1}, respectively, whereas 1, 3, 5, 6, and 8 wt% g-C$_3$N$_4$@ZIF-67 composites had a Tafel value of 173 mV dec^{-1}, 165 mV dec^{-1}, 169 mV dec^{-1}, 170 mV dec^{-1} and 210 mV dec^{-1} respectively while 5% Pt/c attain Tafel slope 58 mV dec^{-1}. The Tafel slope values of HER exhibited similar results as predicted from LSV data; 3 wt% g-C$_3$N$_4$/ZIF-67 MOF attained better kinetics as compared to other designed electrocatalyst.
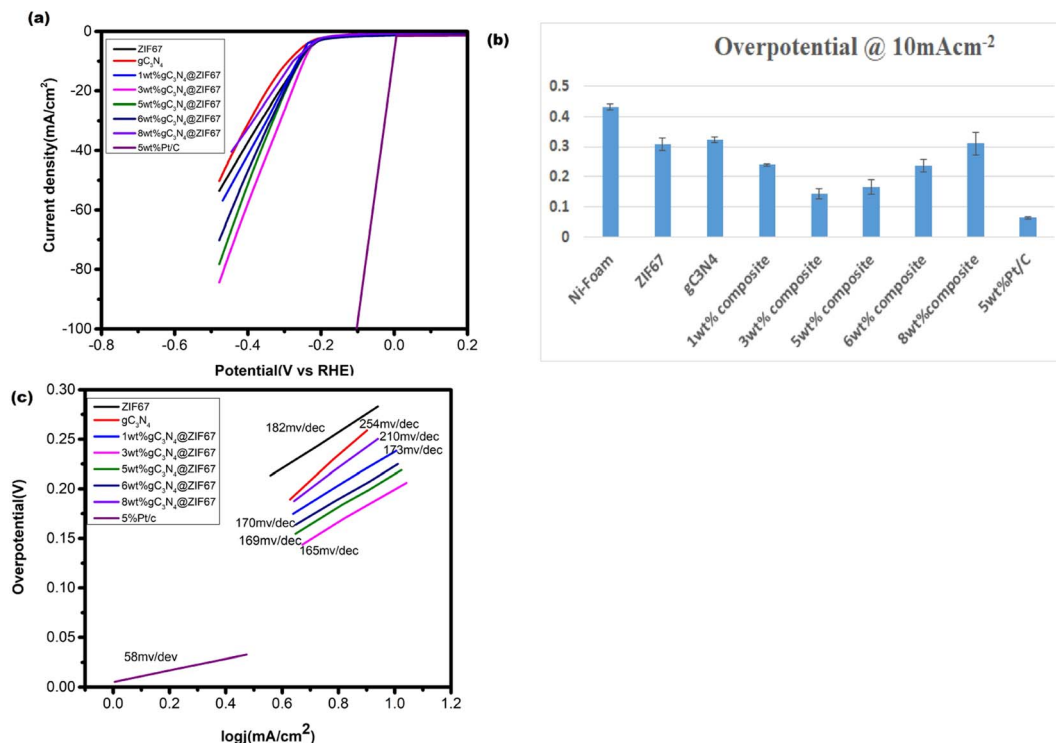
Fig. 8 (a) LSV curve of pure ZIF-67 MOF and 1, 3, 5, 6, 8 wt% g-C$_3$N$_4$ composites in the alkaline media @ 10 mV s^{-1} (b) overpotential bar graph@10 mA cm^{-2} (c) Tafel slope corresponding to HER.

3.2. Oxygen evolution reaction

The OER performance of the designed electrocatalyst is also examined by the LSV curve under the alkaline environment and compared with bare Ni-foam and commercially available IrO$_2$, as illustrated in Fig. 9a. Results reveal that Ni-Foam could not attain the current density of 10 mA cm^{-2} while the LSV OER
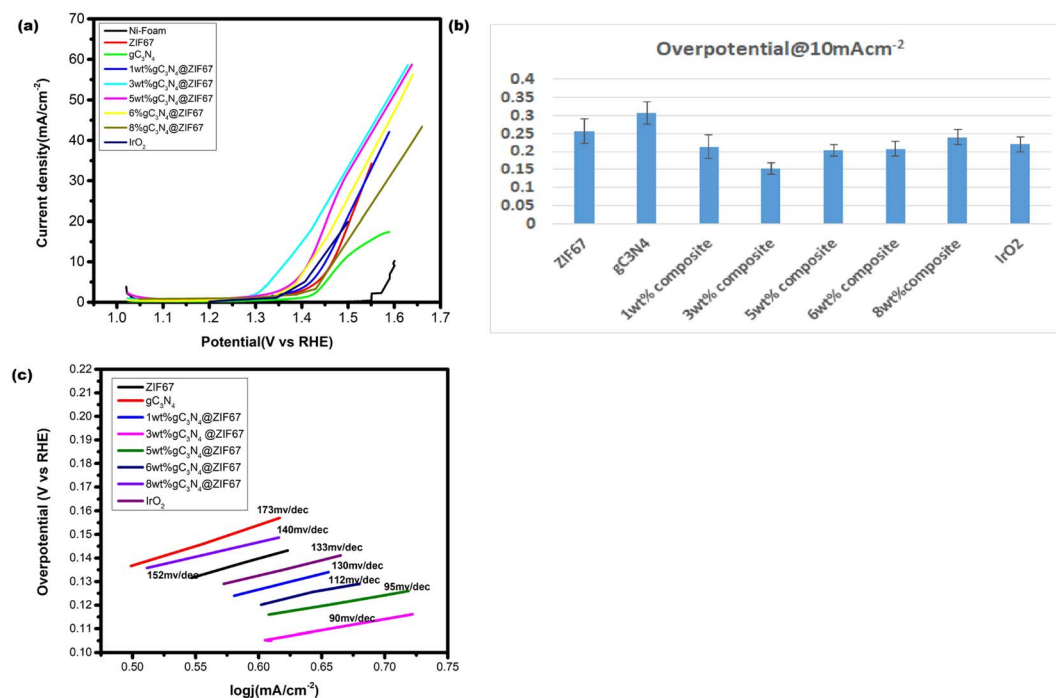

Fig. 9 (a) LSV curve of ZIF-67 and 1, 3, 5, 6, 8 wt% g-C$_3$N$_4$ composites in the alkaline media @ 10 mV s^{-1} (b) overpotential bar graph of the catalysts at "current density" 10 mA cm^{-2} (c) Tafel slop corresponding to OER.

polarization curve represents the activity differentiations after adding different weight% of g-C$_3$N$_4$. The composite material's current density also enhances, notably 3 wt% g-C$_3$N$_4$ composite raises abruptly after the 1.3 V. The overpotential of electrocatalysts is calculated at 10 and 30 mA cm^{-2}. The low overpotential is required for ZIF-67 (0.256 V), g-C$_3$N$_4$ (0.306 V), 1 wt% g-C$_3$N$_4$ composite (0.213 V), 3 wt% g-C$_3$N$_4$ composite (0.152) 5 wt% g-C$_3$N$_4$ composite (0.20 V), 6 wt% g-C$_3$N$_4$ composite (0.21 V), 8 wt% g-C$_3$N$_4$ composite (0.24 V) and IrO$_2$ (0.22 V) to achieve the current density 10 mA cm^{-2}. It is observed that the 1 wt% and 5 wt% g-C$_3$N$_4$ composite illustrate overpotential near to commercial catalyst while 3 wt% g-C$_3$N$_4$@ZIF-67 composite remained superior to all others. Similarly results attained at 30 mA cm^{-2} the overpotential value is required for ZIF-67 (0.30 V), 1 wt% g-C$_3$N$_4$ composite (0.28 V), 3 wt% g-C$_3$N$_4$ composite (0.239 V), 5 wt% g-C$_3$N$_4$ composite

(0.266 V), 6 wt% g-C$_3$N$_4$ composite (0.279 V), and 8 wt% g-C$_3$N$_4$ composite (0.31 V).

Tafel graphs for OER are also investigated to evaluate the kinetics of catalysts, as shown in Fig. 9c. 3 wt% g-C$_3$N$_4$ composite with ZIF-67 revealed less value 90 mV dec^{-1}, as compare to pure ZIF-67 (152 mV dec^{-1}), g-C$_3$N$_4$ (173 mV dec^{-1}) 1 wt% (133 mV dec^{-1}), 5 wt% (95 mV dec^{-1}), 6 wt% (112 mV dec^{-1}),8 wt% (140 mV dec^{-1}) g-C$_3$N$_4$/ZIF-67 and IrO$_2$ (130 mV dec^{-1}).

Results of LSV OER is revealed after the combination of g-C$_3$N$_4$ with ZIF-67, 3 wt% depicted a remarkable catalyst activity with low overpotential achieved as compared to IrO$_2$ as mentioned in Fig. 9b. Designed catalyst also compare with other designed material for OER activity which are summarized in Table S1†.[36,79–84] The experimental results demonstrate that the integration of ZIF-67 with g-C$_3$N$_4$ facilitates effective electron transfer from atomic cobalt (Co) to a nitrogen-doped graphitic
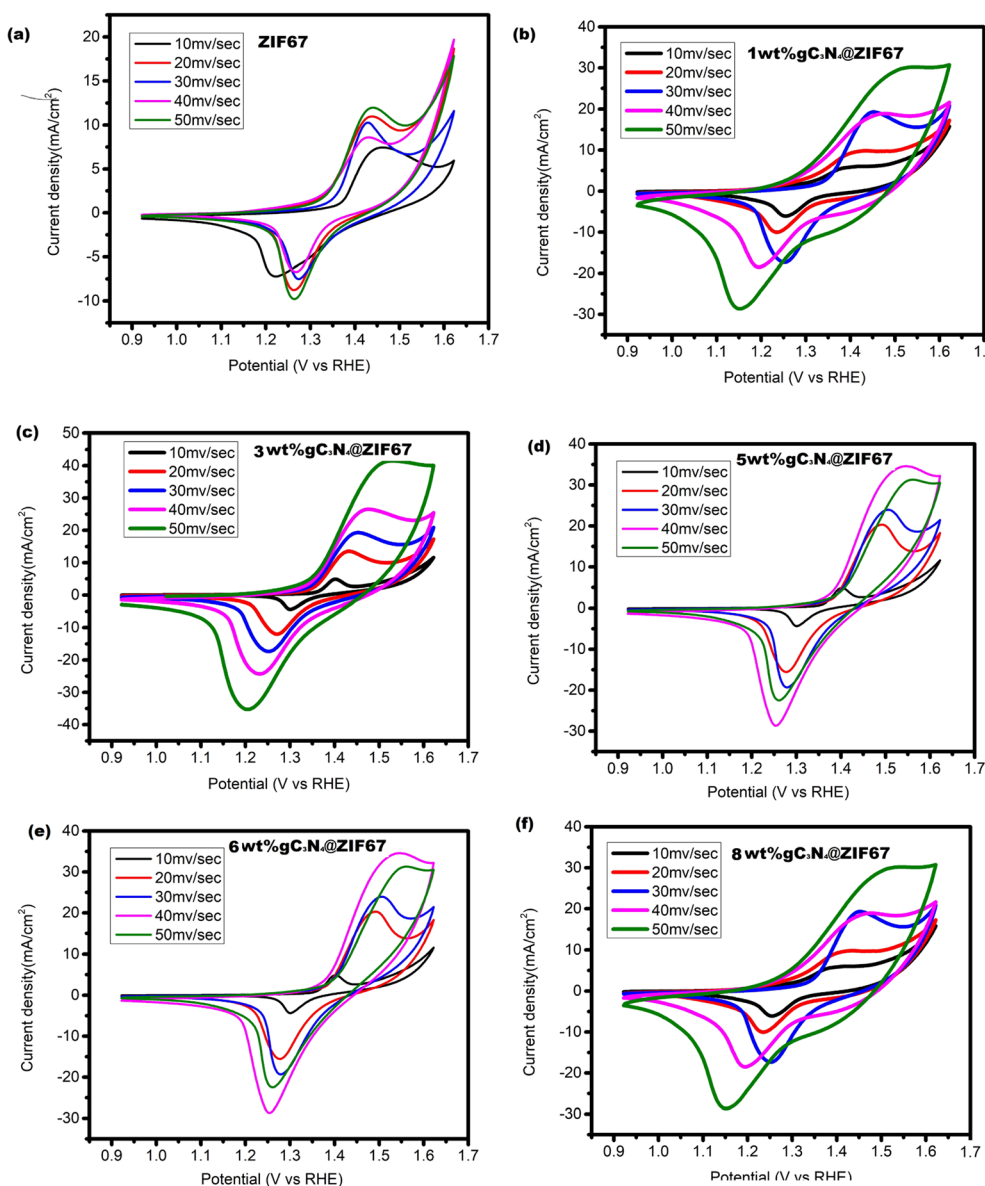

Fig. 10 Cyclic voltammogram of pure ZIF-67 and 1, 3, 5 wt% g-C$_3$N$_4$ composite@10 mV sec^{-1}.

carbon framework. This synergistic combination promotes enhanced electron mobility within the catalyst system, and contributing to its improved catalytic performance. Furthermore, the porous nature of composite material plays a crucial role in the catalytic process. The active sites in the porous structure facilitates efficient diffusion of reactants to the catalytic sites and leading to enhanced catalytic activity. Moreover, the porous architecture facilitates easy desorption of reaction products, further promoting the overall efficiency of the catalyst. From the OER polarization curve, it is also noticed that when the concentration of g-C_3N_4 increased 5, 6, 8 wt% in the MOF, the overpotential increased as compared to 3 wt% g-C_3N_4 because exceeding the quantity of carbon-based material from the appropriate limit catalyst hindered the active sites and its porous network agglomerate the surface which reduced the activity of the catalyst.[50]

Cyclic voltammetry experiments are conducted to analyze the current density and scan rate characteristics of ZIF-67 and its composites with 1, 3, 5, 6 and 8 wt% g-C_3N_4. The cyclic voltammograms for these materials are obtained at scan rates ranging from 10 to 50 mV s^{-1}. The recorded curves exhibited distinct redox peaks within the potential range of 0.9–1.7 V *vs.* RHE, indicating a B-type behavior. A comparison of the cyclic voltammograms between ZIF-67, 1 wt% g-C_3N_4@ZIF-67, 3 wt% g-C_3N_4@ZIF-67, 5 wt% g-C_3N_4@ZIF-67, 6 wt% g-C_3N_4@ZIF-67, 8 wt% g-C_3N_4@ZIF-67 revealed noticeable differences in the current densities as shown in Fig. 10. At a scan rate of 50 mV s^{-1}, the anodic peak currents for ZIF-67, 1 wt% g-C_3N_4@ZIF-67, 3 wt% g-C_3N_4@ZIF-67, 5 wt% g-C_3N_4@ZIF-67, 6 wt% g-C_3N_4@ZIF-67, 8 wt% g-C_3N_4@ZIF-67 are measured as 11.87 mA, 29.9 mA, 40.4 mA, 44.7 mA, 34.14 mA 32.1 mA and 30.4 mA respectively. Similarly, the cathodic peak currents for the same samples are recorded as −9.6 mA, −28.44 mA, −37.2 mA, −35.08 mA, −28.7 mA, −27.6 mA and −25.8 mA. The obtained results demonstrate that the cyclic voltammograms of all samples maintain a stable curve shape even with increasing scan rates,
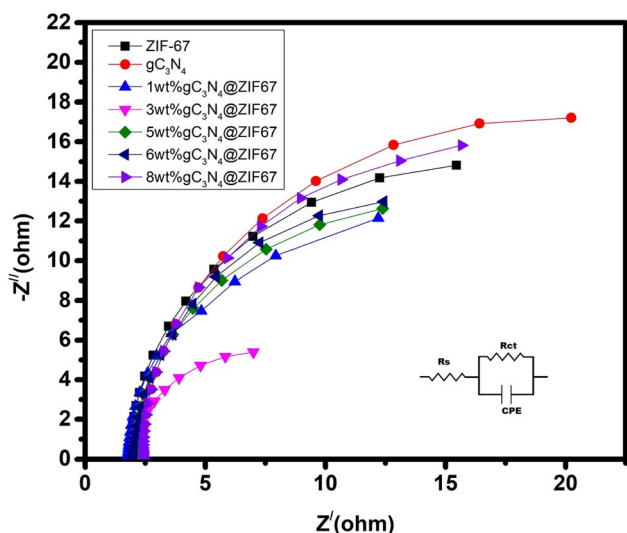
Table 2 Representing solution resistance, charge transfer resistance, and capacitance of ZIF-67 and 1, 3, 5, 6, 8 wt% composites of g-C_3N_4@ZIF-67 MOF

Catalyst	R_p (ohm)	R_{ct} (ohm)	Capacitance (F)
ZIF-67	36.6	6.666	3.611×10^{-3}
1 wt% g-C_3N_4@ZIF-67	23.2	6.174	4.47×10^{-3}
3 wt% g-C_3N_4@ZIF-67	18.4	5.64	5.852×10^{-3}
5 wt% g-C_3N_4@ZIF-67	19.7	7	4.770×10^{-3}
6 wt% g-C_3N_4@ZIF-67	20.4	8.5	4.070×10^{-3}
8 wt% g-C_3N_4@ZIF-67	24.6	16.666	3.666×10^{-3}

indicating good cyclic stability and lower electrocatalyst resistance. Additionally, it is observed that the introduction of a slightly increased quantity of g-C_3N_4 affected the electrochemical behavior by causing π–π interactions and reducing the active surface area, leading to a slower kinetic response of the electrocatalyst.[29] Nevertheless, the appropriate combination of active materials with the substrate enhances the overall activity.

EIS is investigated at a fixed potential of 0.2 V (*vs.* Ag/AgCl) under the frequency range of 100 kHz to 0.1 Hz. In order to measure the well-fitting of the Nyquist plot, the Randle circuit model was appropriately fitted on the plot; the model is inset in Fig. 11. The semicircle plot parameter results are illustrated in Table 2. The real and imaginary impedance plots reveal a tiny semicircle at a low-frequency section that correlates with Rct (charge transfer resistance). It illustrated that 3 wt% g-C_3N_4-ZIF-67 MOF performed better and had the lowest charge transfer resistance value compared to the other materials, which significantly impacts impedance as it prevents the increase of charge resistance.

The long-term stability of an efficient catalyst (3 wt% g-C_3N_4@ZIF-67) is also measured in the alkaline media, which is also an essential key factor in evaluating the catalyst's performance. The chronopotentiometry was measured at a fixed potential of 0.01 V (*vs.* Ag/AgCl) for 24 h. The result indicates
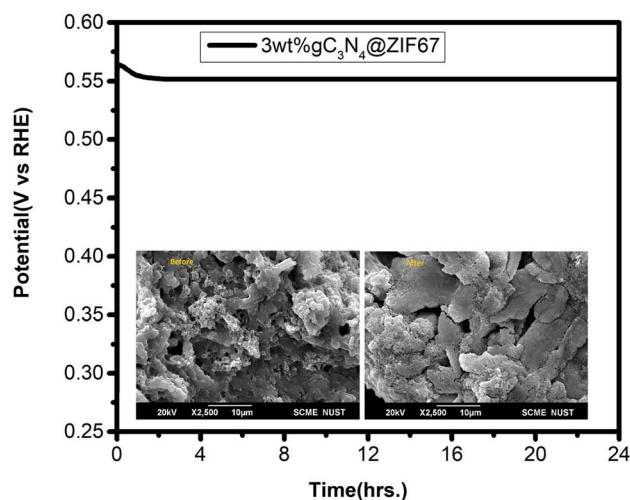

Fig. 11 EIS (Nyquist) plot for OER of ZIF-67 and 1, 3, 5, 6, 8 wt% composites of g-C_3N_4@ZIF-67 MOF.

Fig. 12 Chronopotentiometry graph 3 wt% g-C_3N_4@ZIF-67 MOF with (inset: SEM before and after stability).
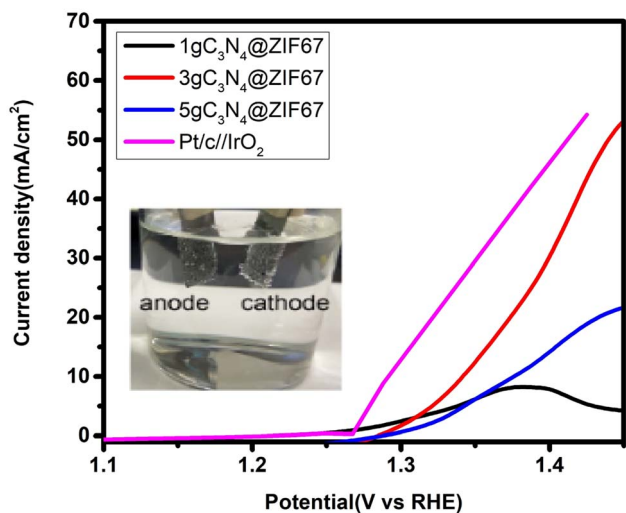
Fig. 13 Overall water splitting of Pt/c//IrO$_2$ and 1, 3, 5 wt% composites in alkaline media.

robust stability with minimal degradation of current (20%). Moreover, SEM is performed before and after stability, as shown in Fig. 12. SEM results showed that the catalyst remained stable on Ni foam after 24 h stability test. The high stability and lower overpotential observed in the 3 wt% g-C$_3$N$_4$@ZIF-67 catalyst suggest its promising potential as an electrocatalyst with dual functions for the hydrogen evolution reaction (HER) and oxygen evolution reaction (OER). This makes it an attractive candidate for water-splitting applications in alkaline.

The comparative study of the synthesized material with the already reported material is illustrated in Table S1 (ESI†). Among the designed materials and reported catalysts, the 3 wt% g-C$_3$N$_4$/ZIF-67 composite demonstrated the most promising results. This superior performance can be attributed to the optimal loading of g-C$_3$N$_4$, which effectively encapsulated the ZIF-67 MOF, and provide a sufficient surface area for charge transportation within the composite. The presence of an appropriate amount of g-C$_3$N$_4$ ensures the formation of active sites and accessible pores, leading to improved catalytic efficiency. Furthermore, it also observed that the 5, 6, 8 wt% g C$_3$N$_4$ on the ZIF-67 increased the overpotential for HER and OER, which is possibly an overdose of graphitic-carbon nitride (g-C$_3$N$_4$) on the ZIF-67 surface that adhered the active surface area of the catalyst and reduced the catalytic efficiency.[85,86]

3.3. Overall water-splitting

After the fascinating from the OER and HER results, we performed the overall water-splitting activity, as shown in Fig. 13. Therefore, a two-electrode setup is a buildup based on the bifunctional 3 wt% composites for overall water splitting. 3 wt% composites of graphitic carbon nitride and ZIF-67 are used as the anode and cathode under alkaline media (1 M KOH) for overall water electrolysis. The performance of 3 wt% composite is also compare with 1, 5 wt% g-C$_3$N$_4$@ZIF and Pt/C//IrO$_2$. The results of overall water splitting reveal that cell potential at 10 mA cm^{-2} is 1.34 V for 3 wt% and for 5 wt% 1.4 V, while 1 wt% did not reach the current density at 10 mA cm^{-2}. This may be because 1 wt% g-C$_3$N$_4$ catalysts have a lower amount of graphite carbon nitride (g-C$_3$N$_4$), which makes it more likely to be less stable and degraded at higher potentials. As a result, its catalytic activity decreases as the reaction goes on.[43,87] Meanwhile, commercial catalyst 5 wt% Pt/c//IrO$_2$ attained 1.29 V potential at 10 mA cm^{-2} which is nearly close to 3 wt% g-C$_3$N$_4$@ZIF67.

3.4. Contact angle test synthesized catalysts

Wettability is another crucial technique to verify the proficiency of the catalyst for water-splitting application. Ni-foam is hydrophobic in nature and makes a high contact angle (<95°) between liquid and solid, which the naked eye can see. The
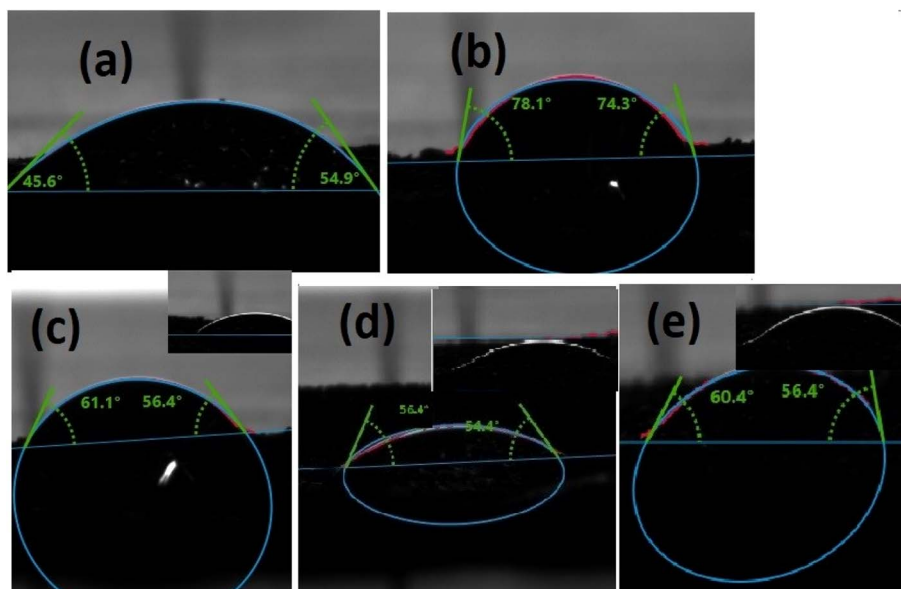

Fig. 14 Contact angle of (a) ZIF-67, (b) g-C$_3$N$_4$ (c) 1 wt%, (d) 3 wt% (e) 5 wt% g-C$_3$N$_4$/ZIF-67.

contact angle between the liquid and solid surface ensures the wettability of the electrocatalyst.[88,89] A hydrophilic substance can easily make a wetting film on the surface of the electrode, which enhances the contact between the electrode and electrolyte. Moreover, hydrophilic catalysts reduced the accumulation of gas bubbles, which adhere to the contact between the electrode and electrolyte. Thus, the wettability phenomenon demonstrates that the more hydrophilic nature of the catalyst promotes hydrolysis activity.[90]

As shown in Fig. 14, the contact angle of g-C_3N_4 showed a large angle of 78.1° ± 2 compared to ZIF-67 54.9° ± 2, which described that g-C_3N_4 is hydrophobic compared to ZIF-67. Moreover, when the electrolyte droplet touched with 1 wt%, 3 wt%, and 5 wt% composites, the contact angles are 61.1°, 54.4°, and 60.4°, respectively. These results illustrated that 3 wt% composite attributed high wettability due to the low contact angle and showed excellent hydrophilic nature.

4. Conclusion

In our research, we designed the composites 1, 3, 5, 6 and 8 wt% g-C_3N_4@ZIF-67 by hydrothermal method. The morphology of the catalyst are examined by XRD, SEM, FTIR and BET. The electrochemical activity of the catalyst is done by LSV, Tafel slope value, EIS and CV and compare their catalyst activity with commercial catalyst; 5 wt% Pt/c and IrO_2. Result shows that 3 wt% g-C_3N_4@ZIF-67 composite outperforms with a lower "overpotential" 0.176 V and 0.152 V for the OER and HER, in the alkaline environment. The combination of g-C_3N_4 with ZIF-67 provides a large active surface area, promoting charge transfer in the composite, and enhance the stability of the catalyst. The catalyst activity also investigates for the overall water splitting application, where 3 wt% g-C_3N_4/ZIF-67 performed outstandingly in an alkaline. In conclusion, for water splitting application numerous catalyst have been explored. Still facing the challenges towards less conductivity and low catalyst activity towards electrochemical water splitting application. Although many of the catalyst are discovered for HER and OER but more work is needed to lower the overpotential and improve the overall water-splitting application. This research gives insight into developing an electrocatalyst for overall water-splitting application.

Conflicts of interest

There are no conflicts to declare.

Acknowledgements

References

1 M. Ali and E. Pervaiz, Effect of synthesis route on electrocatalytic water-splitting activity of MoS2/UiO-66 hybrid, *Mol. Catal.*, 2022, **519**, 112136.

2 W. Liu, *et al.*, Non-noble metal single-atom catalysts prepared by wet chemical method and their applications in electrochemical water splitting, *J. Energy Chem.*, 2020, **47**, 333–345.

3 M. Ali, *et al.*, Recent advancements in MOF-based catalysts for applications in electrochemical and photoelectrochemical water splitting: A review, *Int. J. Energy Res.*, 2021, **45**(2), 1190–1226.

4 Y. Ma, *et al.*, Highly Enhanced OER Performance by Er-Doped Fe-MOF Nanoarray at Large Current Densities, *Nanomaterials*, 2021, **11**(7), 1847.

5 X. Zhang, *et al.*, High-performance MoC electrocatalyst for hydrogen evolution reaction enabled by surface sulfur substitution, *ACS Appl. Mater. Interfaces*, 2021, **13**(34), 40705–40712.

6 A. M. Oliveira, R. R. Beswick and Y. Yan, A green hydrogen economy for a renewable energy society, *Curr. Opin. Chem. Eng.*, 2021, **33**, 100701.

7 M. Frenkel-Pinter, *et al.*, Water and life: The medium is the message, *J. Mol. Evol.*, 2021, **89**(1), 2–11.

8 S. Chen, T. Takata and K. Domen, Particulate photocatalysts for overall water splitting, *Nat. Rev. Mater.*, 2017, **2**(10), 1–17.

9 A. Sajid, *et al.*, A perspective on development of fuel cell materials: Electrodes and electrolyte, *Int. J. Energy Res.*, 2022, **46**(6), 6953–6988.

10 S. A. M. Rizvi, *et al.*, Synthesis and characterization of Cu-MOF derived Cu@ AC electrocatalyst for oxygen reduction reaction in PEMFC, *Catal. Lett.*, 2020, **150**, 1397–1407.

11 T. Noor, Y. Qi and D. Chen, Hydrogen dependence of the reaction mechanism and kinetics of water gas shift reaction on Ni catalyst: Experimental and DFT study, *Appl. Catal., B*, 2020, **264**, 118430.

12 N. Zaman, T. Noor and N. Iqbal, Recent advances in the metal–organic framework-based electrocatalysts for the hydrogen evolution reaction in water splitting: a review, *RSC Adv.*, 2021, **11**(36), 21904–21925.

13 L. Wu, Z. Xi, and S. Sun, Chapter 4 - Well-Defined Metal Nanoparticles for Electrocatalysis, in *Studies in Surface Science and Catalysis*, ed. P. Fornasiero and M. Cargnello, Elsevier, 2017, pp. 123–148.

14 H. Zhou, *et al.*, Water splitting by electrolysis at high current densities under 1.6 volts, *Energy Environ. Sci.*, 2018, **11**(10), 2858–2864.

15 U. A. Asif, *et al.*, LSTN (La0.4Sr0.4Ti0.9Ni0.1O3-&) perovskite and graphitic carbon nitride (g-C3N4) hybrids as a bifunctional electrocatalyst for water-splitting applications, *J. Alloys Compd.*, 2023, **939**, 168668.

16 T. Noor, L. Yaqoob and N. Iqbal, Recent advances in electrocatalysis of oxygen evolution reaction using noble-metal, transition-metal, and carbon-based materials, *ChemElectroChem*, 2021, **8**(3), 447–483.

17 R. Maric and H. Yu, Proton exchange membrane water electrolysis as a promising technology for hydrogen production and energy storage. *Nanostructures in energy generation, transmission and storage*, 2019: p. 13.

18 F. Hess, B. M. Smarsly and H. Over, Catalytic stability studies employing dedicated model catalysts, *Acc. Chem. Res.*, 2020, **53**(2), 380–389.

19 A. Hanan, *et al.*, Co2FeO4@rGO composite: Towards trifunctional water splitting in alkaline media, *Int. J. Hydrogen Energy*, 2022, **47**(80), 33919–33937.

20 D. Wang, *et al.*, N, P (S.) Co-doped Mo2C/C hybrid electrocatalysts for improved hydrogen generation, *Carbon*, 2018, **139**, 845–852.

21 G. Liu, *et al.*, Engineering Ir and Ni3N heterogeneous interfaces for promoted overall water splitting, *Appl. Surf. Sci.*, 2023, **637**, 157896.

22 X. Zhang, *et al.*, Structure and phase regulation in MoxC (α-MoC1-x/β-Mo2C) to enhance hydrogen evolution, *Appl. Catal., B*, 2019, **247**, 78–85.

23 T. Liu, *et al.*, Boosted hydrogen evolution from α-MoC1-x-MoP/C heterostructures, *Electrochim. Acta*, 2020, **334**, 135624.

24 A. Ahmad, *et al.*, Cu-doped zeolite imidazole framework (ZIF-8) for effective electrocatalytic CO2 reduction, *J. CO2 Util.*, 2021, **48**, 101523.

25 R. Mehek, *et al.*, Metal–organic framework based electrode materials for lithium-ion batteries: a review, *RSC Adv.*, 2021, **11**(47), 29247–29266.

26 M. Usman, *et al.*, Advanced Strategies in Metal-Organic Frameworks for CO2 Capture and Separation, *Chem. Rec.*, 2022, **22**(7), e202100230.

27 M. Ali, E. Pervaiz and O. Rabi, Enhancing the overall electrocatalytic water-splitting efficiency of Mo2C nanoparticles by forming hybrids with UiO-66 MOF, *ACS omega*, 2021, **6**(50), 34219–34228.

28 L. Yaqoob, *et al.*, Electrochemical synergies of Fe–Ni bimetallic MOF CNTs catalyst for OER in water splitting, *J. Alloys Compd.*, 2021, **850**, 156583.

29 L. Yaqoob, *et al.*, Nanocomposites of cobalt benzene tricarboxylic acid MOF with rGO: An efficient and robust electrocatalyst for oxygen evolution reaction (OER), *Renewable Energy*, 2020, **156**, 1040–1054.

30 W. Han, *et al.*, Cobalt-based metal-organic frameworks and their derivatives for hydrogen evolution reaction, *Front. Chem.*, 2020, **8**, 592915.

31 K. C. Devarayapalli, *et al.*, Nanostructured cobalt-based metal-organic framework/cadmium sulfide electrocatalyst for enhanced oxygen evolution reaction and anion exchange membrane-based water electrolysis: Synergistic effect, *J. Power Sources*, 2022, **527**, 231151.

32 Y. Yang, *et al.*, Self-supported ZIF-coated Co2P/V3P bifunctional electrocatalyst for high-efficiency water splitting, *J. Ind. Eng. Chem.*, 2022, **110**, 587–597.

33 S. R. Naqvi, *et al.*, Catalytic Pyrolysis Of Botryococcus Braunii (microalgae) Over Layered and Delaminated Zeolites For Aromatic Hydrocarbon Production, *Energy Procedia*, 2017, **142**, 381–385.

34 R. Qiang, *et al.*, Electromagnetic functionalized Co/C composites by *in situ* pyrolysis of metal-organic frameworks (ZIF-67), *J. Alloys Compd.*, 2016, **681**, 384–393.

35 N. Zaman, N. Iqbal and T. Noor, Comparative study of Mn-ZIF-67 derived carbon (Mn-Co/C) and its rGO-based composites for the methanol oxidation, *J. Environ. Chem. Eng.*, 2022, **10**(5), 108351.

36 Y. Wang, *et al.*, Facile synthesis of silver nanowire-zeolitic imidazolate framework 67 composites as high-performance bifunctional oxygen catalysts, *Nanoscale*, 2018, **10**(33), 15755–15762.

37 X. Guo, G. Liang and A. Gu, Designed formation of CoS2 nanoboxes with enhanced oxygen evolution reaction electrocatalytic properties, *Int. J. Hydrogen Energy*, 2019, **44**(59), 31020–31028.

38 Z. Liang, *et al.*, Metallic 1T-phase MoS 2 quantum dots/gC 3 N 4 heterojunctions for enhanced photocatalytic hydrogen evolution, *Nanoscale*, 2019, **11**(25), 12266–12274.

39 B. Zhang, *et al.*, Improving hydrogen evolution reaction performance by combining ditungsten carbide and nitrogen-doped graphene: A first-principles study, *Carbon*, 2021, **172**, 122–131.

40 B. Fang, *et al.*, Dense Pt Nanowire Electrocatalyst for Improved Fuel Cell Performance Using a Graphitic Carbon Nitride-Decorated Hierarchical Nanocarbon Support, *Small*, 2021, **17**(30), 2102288.

41 H. Yu, *et al.*, Smart utilization of carbon dots in semiconductor photocatalysis, *Adv. Mater.*, 2016, **28**(43), 9454–9477.

42 S. Cao, *et al.*, Polymeric photocatalysts based on graphitic carbon nitride, *Adv. Mater.*, 2015, **27**(13), 2150–2176.

43 B. Fang, *et al.*, Upgrading the State-of-the-Art Electrocatalysts for Proton Exchange Membrane Fuel Cell Applications, *Adv. Mater. Interfaces*, 2022, **9**(17), 2200349.

44 S. Wang, *et al.*, Nanocoral-like composite of nickel selenide nanoparticles anchored on two-dimensional multi-layered graphitic carbon nitride: A highly efficient electrocatalyst for oxygen evolution reaction, *Appl. Catal., B*, 2019, **243**, 463–469.

45 Y. Zhou, *et al.*, A three-dimensional self-standing Mo2C/nitrogen-doped graphene aerogel: enhancement hydrogen production from landfill leachate wastewater in MFCs-AEC coupled system, *Environ. Res.*, 2020, **184**, 109283.

46 Y. Li, *et al.*, Fabrication of ternary AgBr/BiPO4/g-C3N4 heterostructure with dual Z-scheme and its visible light photocatalytic activity for Reactive Blue 19, *Environ. Res.*, 2021, **192**, 110260.

47 H. Che, *et al.*, Nitrogen doped carbon ribbons modified g-C3N4 for markedly enhanced photocatalytic H2-production in visible to near-infrared region, *Chem. Eng. J.*, 2020, **382**, 122870.

48 S. Kumar, *et al.*, Two-dimensional carbon-based nanocomposites for photocatalytic energy generation and environmental remediation applications, *Beilstein J. Nanotechnol.*, 2017, **8**(1), 1571–1600.

49 Y. Li, *et al.*, FeS2 bridging function to enhance charge transfer between MoS2 and g–C3N4 for efficient hydrogen evolution reaction, *Chem. Eng. J.*, 2021, **421**, 127804.

50 R. Zahra, *et al.*, Three-dimensional hierarchical flowers-like cobalt-nickel sulfide constructed on graphitic carbon

nitride: Bifunctional non-noble electrocatalyst for overall water splitting, *Electrochim. Acta*, 2022, **418**, 140346.

51 Y. Meng, *et al.*, Construction of g-C3N4/ZIF-67 photocatalyst with enhanced photocatalytic CO2 reduction activity, *Mater. Sci. Semicond. Process.*, 2019, **95**, 35–41.

52 J. Qian, F. Sun and L. Qin, Hydrothermal synthesis of zeolitic imidazolate framework-67 (ZIF-67) nanocrystals, *Mater. Lett.*, 2012, **82**, 220–223.

53 H.-S. Zhai, L. Cao and X.-H. Xia, Synthesis of graphitic carbon nitride through pyrolysis of melamine and its electrocatalysis for oxygen reduction reaction, *Chin. Chem. Lett.*, 2013, **24**(2), 103–106.

54 S. Sundriyal, *et al.*, Enhanced electrochemical performance of nickel intercalated ZIF-67/rGO composite electrode for solid-state supercapacitors, *Int. J. Hydrogen Energy*, 2020, **45**(55), 30859–30869.

55 M. Abbasi, *et al.*, Electrocatalytic study of cu/Ni MOF and its g-C3N4 composites for methanol oxidation reaction, *Int. J. Energy Res.*, 2022, **46**(10), 13915–13930.

56 Y. Li, *et al.*, Bimetallic zeolitic imidazolite framework derived carbon nanotubes embedded with Co nanoparticles for efficient bifunctional oxygen electrocatalyst, *Adv. Energy Mater.*, 2018, **8**(9), 1702048.

57 S.-J. Huang, *et al.*, Two-Dimensional Layered NiLiP2S6 Crystals as an Efficient Bifunctional Electrocatalyst for Overall Water Splitting, *Catalysts*, 2021, **11**(7), 786.

58 H. Wen, *et al.*, ZIF-67-based catalysts for oxygen evolution reaction, *Nanoscale*, 2021, **13**(28), 12058–12087.

59 S. Ghoshal, *et al.*, ZIF 67 based highly active electrocatalysts as oxygen electrodes in water electrolyzer, *ACS Appl. Energy Mater.*, 2019, **2**(8), 5568–5576.

60 H. Dai, *et al.*, Highly photoactive heterojunction based on g-C3N4 nanosheets decorated with dendritic zinc (II) phthalocyanine through axial coordination and its ultrasensitive enzyme-free sensing of choline, *RSC Adv.*, 2014, **4**(102), 58226–58230.

61 M. Abbasi, T. Noor, N. Iqbal and N. Zaman, Electrocatalytic study of cu/Ni MOF and its g-C3N4 composites for methanol oxidation reaction, *Int. J. Energy Res.*, 2022, **46**(10), 13915–13930.

62 S. Sundriyal, *et al.*, High-performance symmetrical supercapacitor with a combination of a ZIF-67/rGO composite electrode and a redox additive electrolyte, *ACS omega*, 2018, **3**(12), 17348–17358.

63 H.-J. Li, *et al.*, Preparation of water-dispersible porous gC 3 N 4 with improved photocatalytic activity by chemical oxidation, *Phys. Chem. Chem. Phys.*, 2015, **17**(5), 3309–3315.

64 D. R. Paul, *et al.*, ZnO-modified g-C3N4: a potential photocatalyst for environmental application, *ACS omega*, 2020, **5**(8), 3828–3838.

65 J. Goetze, *et al.*, Revealing lattice expansion of small-pore zeolite catalysts during the methanol-to-olefins process using combined operando X-ray diffraction and UV–vis spectroscopy, *ACS Catal.*, 2018, **8**(3), 2060–2070.

66 Y. Hu, *et al.*, Zeolitic imidazolate framework-67 for shape stabilization and enhanced thermal stability of paraffin-based phase change materials, *RSC Adv.*, 2019, **9**(18), 9962–9967.

67 K. Zhou, *et al.*, Characterization and properties of Zn/Co zeolitic imidazolate frameworks *vs.* ZIF-8 and ZIF-67, *J. Mater. Chem. A*, 2017, **5**(3), 952–957.

68 J. Cheng, *et al.*, Facile synthesis of g-C3N4/BiVO4 heterojunctions with enhanced visible light photocatalytic performance, *Ceram. Int.*, 2017, **43**(1), 301–307.

69 H. Hayat, *et al.*, Electrocatalytic activity of Cu MOF and its g-C3N4-based composites for oxygen reduction and evolution reaction in metal-air batteries, *J. Environ. Chem. Eng.*, 2023, **11**(3), 109627.

70 A. U. Khan, *et al.*, CO2 adsorption study of the zeolite imidazolate framework (ZIF-8) and its g-C3N4 composites, *J. Mater. Sci.*, 2023, **58**(9), 3947–3959.

71 B. L. Phoon, *et al.*, Highly mesoporous g-C3N4 with uniform pore size distribution *via* the template-free method to enhanced solar-driven tetracycline degradation, *Nanomaterials*, 2021, **11**(8), 2041.

72 R. Banerjee, *et al.*, High-throughput synthesis of zeolitic imidazolate frameworks and application to CO2 capture, *Science*, 2008, **319**(5865), 939–943.

73 R. C. Pawar, *et al.*, Room-temperature synthesis of nanoporous 1D microrods of graphitic carbon nitride (g-C3N4) with highly enhanced photocatalytic activity and stability, *Sci. Rep.*, 2016, **6**(1), 1–14.

74 G. Zhao, *et al.*, Design of pn homojunctions in metal-free carbon nitride photocatalyst for overall water splitting, *Chin. J. Catal.*, 2021, **42**(3), 501–509.

75 B. Zhu, *et al.*, Fabrication and photocatalytic activity enhanced mechanism of direct Z-scheme g-C3N4/Ag2WO4 photocatalyst, *Appl. Surf. Sci.*, 2017, **391**, 175–183.

76 J. Chen, *et al.*, A 3D Co–CN framework as a high performance electrocatalyst for the hydrogen evolution reaction, *RSC Adv.*, 2016, **6**(48), 42014–42018.

77 H. Ge, *et al.*, Co4N nanoparticles encapsulated in N-doped carbon box as tri-functional catalyst for Zn-air battery and overall water splitting, *Appl. Catal., B*, 2020, **275**, 119104.

78 J.-S. Li, *et al.*, In situ-generated Co@ nitrogen-doped carbon nanotubes derived from MOFs for efficient hydrogen evolution under both alkaline and acidic conditions, *New J. Chem.*, 2017, **41**(19), 10966–10971.

79 W. Zhong, *et al.*, Improved oxygen evolution activity of IrO 2 by *in situ* engineering of an ultra-small Ir sphere shell utilizing a pulsed laser, *Nanoscale*, 2019, **11**(10), 4407–4413.

80 G. Wu, *et al.*, A general synthesis approach for amorphous noble metal nanosheets, *Nat. Commun.*, 2019, **10**(1), 4855.

81 G. Li, *et al.*, Amorphous Yolk–Shelled ZIF-67@ Co3 (PO4) 2 as Nonprecious Bifunctional Catalysts for Boosting Overall Water Splitting, *Inorg. Chem.*, 2021, **60**(19), 14880–14891.

82 L. Xu, *et al.*, Co3O4-anchored MWCNTs network derived from metal-organic frameworks as efficient OER electrocatalysts, *Mater. Lett.*, 2019, **248**, 181–184.

83 Y. Xu, *et al.*, Metal–organic framework–impregnated calixarene-based cluster-derived hierarchically porous bimetallic phosphide nanocomposites for efficient water splitting, *Energy Technol.*, 2020, **8**(5), 2000059.

84 J. Wang, *et al.*, N-functionalized hierarchical carbon composite derived from ZIF-67 and carbon foam for efficient overall water splitting, *J. Ind. Eng. Chem.*, 2022, **105**, 222–230.

85 Y. Zhu, *et al.*, Catalytic activity origin and design principles of graphitic carbon nitride electrocatalysts for hydrogen evolution, *Front. Mater.*, 2019, **6**, 16.

86 N. Mansor, *et al.*, Graphitic carbon nitride as a catalyst support in fuel cells and electrolyzers, *Electrochim. Acta*, 2016, **222**, 44–57.

87 M. Ismael and Y. Wu, A mini-review on the synthesis and structural modification of gC 3 N 4-based materials, and their applications in solar energy conversion and environmental remediation, *Sustainable Energy Fuels*, 2019, **3**(11), 2907–2925.

88 F. Ye, *et al.*, Heterogeneous layered multiple transition metal composite electrocatalysts with controlled composition for hydrogen production, *Int. J. Hydrogen Energy*, 2023, **48**(5), 1733–1746.

89 Q. Zhang, *et al.*, Highly wettable and metallic NiFe-phosphate/phosphide catalyst synthesized by plasma for highly efficient oxygen evolution reaction, *J. Mater. Chem. A*, 2018, **6**(17), 7509–7516.

90 X. Guo, *et al.*, Engineering electron redistribution of bimetallic phosphates with CeO2 enables high-performance overall water splitting, *Chem. Eng. J.*, 2023, **453**, 139796.